2022

Numerical Testcases to Study Proudman Resonance Using Shallow Water Models

Nicole Beisiegel

Jorn Behrens

The 8th European Congress on Computational Methods in Applied Sciences and Engineering
ECCOMAS Congress 2022
5-–9 June 2022, Oslo, Norway

NUMERICAL TESTCASES TO STUDY PROUDMAN RESONANCE USING SHALLOW WATER MODELS

NICOLE BEISIEGEL[1] AND JÖRN BEHRENS[2]

[1] School of Mathematical Sciences
Technological University Dublin
Central Quad CQ-241, Grangegorman Lower
Dublin D07 ADY7, Ireland
e-mail: nicole.beisiegel@tudublin.ie

[2] Department of Mathematics/CEN
Universität Hamburg
Bundesstraße 55
20146 Hamburg, Germany

Key words: Computational Fluid Dynamics, Proudman Resonance, Adaptive Mesh Refinement, Scientific Computing, Discontinuous Galerkin Methods

Abstract. Proudman resonance is the dominant mechanism behind meteotsunamis. We develop a comprehensive set of testcases to validate numerical methods focusing on the performance with respect to represent mentioned resonance. With the test cases we assess the wave amplification in dependence of characteristics of the pressure perturbation, model parameters, model resolution, and bathymetry characteristics. We use the compilation of tests to validate an adaptive discontinuous Galerkin (DG) model for the two-dimensional non-linear shallow water equations. As the tests are highly sensitive to model resolution, we use the adaptive mesh capabilities of the model to locally refine the disturbance and thus gain considerable efficiency.

1 INTRODUCTION

Extreme coastal waves can be triggered by a number of different mechanisms, from extreme winds such as hurricanes, submarine earthquakes, and volcanic eruptions, to localised atmospheric pressure disturbances. In order to develop comprehensive modelling capabilities to protect coastal communities, the understanding of all those mechanisms and their accurate simulation are essential. For this reason, this study focuses on meteotsunamis which are atmospherically induced potentially destructive and extreme waves in the tsunami frequency band. They can be triggered by sudden changes in atmospheric pressures and can be observed in coastal areas. They are a multi-resonant phenomenon, i.e. triggered by a number of resonance mechanisms [14]. The most prominent one being *Proudman* resonance which occurs when travel speeds U of localised atmospheric pressure disturbances are close to the gravity wave speed $\sqrt{gH}$ of the water body, i.e. when Froude numbers $\mathrm{Fr} = \frac{U}{\sqrt{gH}}$ are close to 1.

Although meteotsunamis are not as broadly known and reported about as tsunamis or hurricane storm surge, they are not a niche phenomenon. In the past decade, several events have been reported globally (see also [14]). A number of shelves all over the world exhibit resonant

conditions and potential for meteotsunamis. Due to a dependence on local bathymetries that we will study later, they do not pose a threat to all coastal areas equally. The stepped shelf at the Atlantic Coast of Ireland (see for example [13]) for example rarely experiences meteotsunamis while on the Dutch Coast a meteotsunami event was observed as recently as May 29th, 2017.

As opposed to tsunami which are determined by the seismic source of wave generation, the definition of a meteotsunami is more restrictive. Following the definition proposed in [12], meteotsunamis are atmospherically generated waves that exceed four times the root mean square (rms, or σ) of the wave field. This restriction is necessary in order to exclude non extreme waves that are caused by similar atmospheric forcings such as wind or pressure.

While the main mechanism of such events is known for a long time (see e.g. [18]) modelling and simulation of meteotsunamis have a relatively short history. Triggered by the improvement of tide gauge measurements since the 2004 Boxing Day Tsunami event, there has been an increase in research focused on meteotsunamis (see [16]). However, we are still in the process of understanding and building comprehensive modelling capabilities [6, 11, 24]. A lot of work has been done to understand and simulate Proudman resonances using hydro-dynamical models for example explicit leap frog time models in [10, 12, 20] or WRF forced ROMS simulations as in [17]. Most recently [23] have furthermore investigated the effect of tides on meteotsunami wave generation using idealised test cases using an operational coastal flood model. Due to relatively coarse model resolution, realistic scenarios are widely impractical to date as mentioned in [21]. Analytical test cases presented in the literature focus on linearly sloping beaches as measurement data suggests those to best approximate coastal shelves that are prone to meteotsunami occurrence. Using a state-of-the-art adaptive discontinuous Galerkin model developed and refined in [5, 19] and described briefly in Sec. 2 we present and extend a set of test cases designed to demonstrate a model's capability to reproduce the important aspects of Proudman resonance mechanism in Subsecs. 3.1, to 3.5.

2 METHODS

For this study, we are using the Discontinuous Galerkin (DG) model presented in [5] to simulate Proudman resonances. The model solves the 2D shallow water equations in flux form:

$$\frac{\partial \mathbf{U}}{\partial t} + \nabla \cdot \mathbf{F}(\mathbf{U}) = S(\mathbf{U}) \quad \text{in} \quad \Omega \times T.$$

Here and in the following $\mathbf{U} = (h, h\mathbf{u})^\top$ is an array comprising the water depth h and the 2D momentum $h\mathbf{u}$ with a 2D velocity $\mathbf{u} = (u, v)^\top$ defined on the domain $\Omega \times T$, with $\Omega \subset \mathbb{R}^2$ and T a finite time interval. The spatial coordinates are $\mathbf{x} = (x, y)^\top \in \Omega$, the partial temporal derivative is $\frac{\partial \mathbf{U}}{\partial t}$ and $\nabla \cdot := \left(\frac{\partial}{\partial x}, \frac{\partial}{\partial y}\right) \cdot$ is the divergence operator. The flux tensor $\mathbf{F}$ and source term S are

$$\mathbf{F}(\mathbf{U}) = \begin{bmatrix} h\mathbf{u} \\ h\mathbf{u} \otimes \mathbf{u} + \frac{g}{2} h^2 \mathbf{I}_2 \end{bmatrix}, \quad \text{and} \quad S(\mathbf{U}) = - \begin{bmatrix} 0 \\ gh\nabla b + \boldsymbol{\tau}_C - \rho^{-1} \left(\boldsymbol{\tau}_W + h\nabla p_A + \boldsymbol{\tau}_B\right) \end{bmatrix}, \quad (1)$$

where $g = 9.81$ ms^{-2} is the acceleration due to gravity, $\otimes$ the vector product in 2D, and $\mathbf{I}_2$ the 2×2 identity matrix. The source term comprises a temporally constant bathymetry $b = b(\mathbf{x})$ which we use to define the total height $H(\mathbf{x}, t) = h(\mathbf{x}, t) + b(\mathbf{x})$. Furthermore, S comprises

Coriolis forcing $\boldsymbol{\tau}_C$, a vector-valued wind stress $\boldsymbol{\tau}_W$, the water density ρ, that we assume to be constant, a bottom friction $\boldsymbol{\tau}_B$ that we assume to follow a quadratic Manning law, and the atmospheric pressure p_A. Throughout this paper vector valued quantities are indicated by a bold print while all other quantities are assumed to be scalar.

The computational model in [5] solves a variational form of the system of equations in Eq. (1) using an explicit time integrator with advanced stabilisation techniques for well-balancing and robust wetting and drying at coastlines, described in [19]. It has been extensively tested for idealised hurricane storm surges as well as bench-marked for coastal flooding and seismic tsunami simulations.

It features adaptive mesh capabilities through the grid generator `amatos` described in [3]. This dynamically adaptive mesh refinement is realised through physics-based refinement indicators η_Ω and an iterative process of flagging elements for refinement or coarsening according to indicator maxima until a desired fine resolution is reached. The use of bisection as a refinement strategy furthermore adds to the computational efficiency of the model as it retains space-filling curve orders of elements (see [2] for more detail) which reduces the number of cache misses and, hence, computing time.

3 IDEALISED PROUDMAN RESONANCE

Proudman resonance as first introduced in [15] is the leading mechanism behind meteotsunamis (see [14]). Building on and extending the numerical test cases in [23], we demonstrate the model's capability to simulate this resonance by introducing a set of five test cases, labelled R1 - R5 EXERCISE, that highlight particular aspects:

- R1 EXERCISE in Subsec. 3.1 demonstrates the dependence of wave amplification on the Froude number $\mathrm{Fr} = \frac{U}{\sqrt{gH}}$ with a maximum amplification reached at $\mathrm{Fr} = 1$;
- R2 EXERCISE in Subsec. 3.2 shows that non-linear disturbances with period T_S cause wave amplification that non-linearly depends on T_S;
- R3 EXERCISE in Subsec. 3.3 shows a negative correlation between steepness of linear bathymetry and wave amplification;
- R4 EXERCISE in Subsec. 3.4 shows the importance of spatial resolution of the atmospheric forcing;
- R5 EXERCISE in Subsec. 3.5 shows that stepped bathymetries reduce wave amplification.

The general set-up of the exercises described in Subsecs 3.1-3.5 can be found in Fig. 1 with parameters described in Table 1 and further commented on in the respective paragraph below. All quantities here are in SI base units.

3.1 R1 EXERCISE

This idealised 2D test case was first described in [20] and studies wave amplification caused by a sinusoidal atmospheric depression. The top of Fig.1 depicts the test set-up. In a rectangular domain $\Omega = [0, L]\times[0, \frac{L}{3}]$, with $L = 300{\cdot}10^3$, a leading depression sinusoidal atmospheric pressure

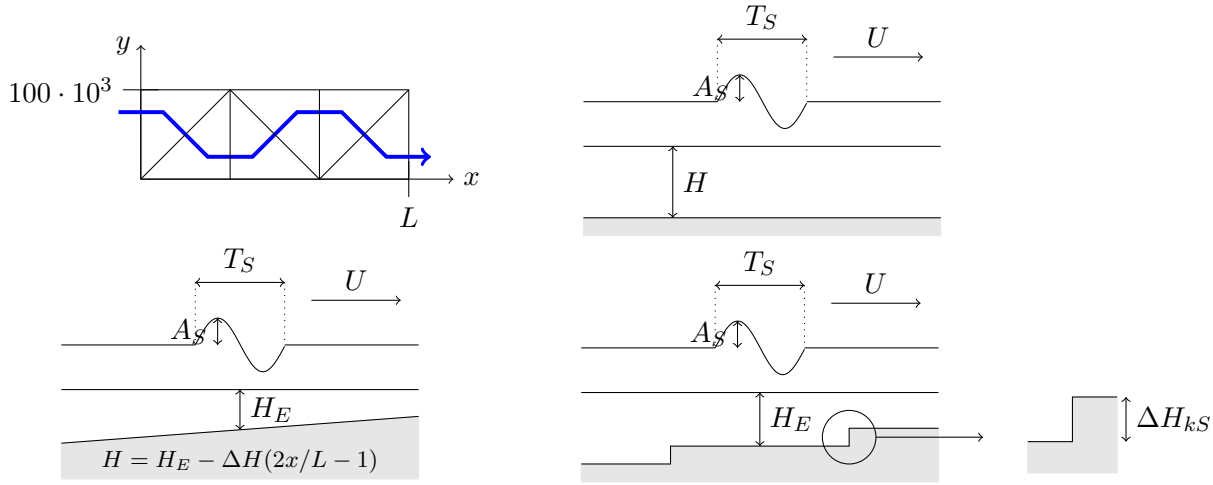

Figure 1: Idealised Proudman Resonance: Macro-triangulation with space-filling curve in blue (top left); Sketches of test set-ups indicating all parameters for R1 and R2 EXERCISE (top right); linearly sloping bathymetry for R3 EXERCISE (bottom left), and stepped bathymetry for R5 EXERCISE (bottom right).

Exercise	H in m	ΔH in m	ΔH_S in m	A_S in hPa	T_s in s	U in m/s	L in m
R1	$[10, 100]$	0	0	1	1800	22.15	$300 \cdot 10^3$
R2	50	0	0	1	$[600, 3600]$	22.15	$300 \cdot 10^3$
R3	50	$[-50, 50]$	0	1	1800	22.15	$81 \cdot 10^3$
R4	50	0	0	1	900	22.15	$[100, 300] \cdot 10^3$
R5	50	0	10	1	900	22.15	$101 \cdot 10^3$

Table 1: Idealised Proudman Resonance: Test parameters for R1, R2, and R3 EXERCISES as in [20] as well as R4 and R5. Where intervals are given, parameter spaces have been equidistantly sampled.

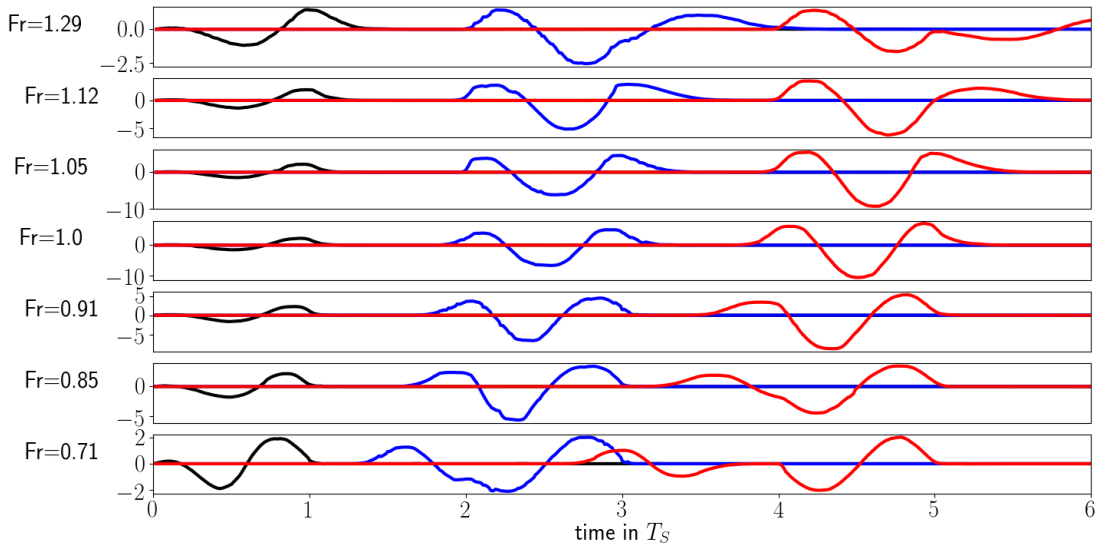

Figure 2: Idealised Proudman Resonance: R1 EXERCISE using different heights H. Depicted are signals measured at gauges G1 (black), G2 (blue), and G3 (red). Vertical scales differ to increase readability.

disturbance, constant in y-direction, of amplitude $A_S = 1$ hPa and period T_S propagates in x-direction at speed U over the basin Ω of depth H. The domain boundaries are assumed to be impermeable at $y \in \{0, \frac{L}{3}\}$, and transmissive at $x \in \{0, L\}$. Manning friction is computed using a Chezy coefficient of $C = 18 \cdot \log(0.37H/z_0)$, where z_0 is the roughness length approximated by $z_0 = 0.003$ and H is the water depth. From C, the Manning coefficient n can be determined by

$$n = \frac{R^{1/6}}{C} \approx \frac{H^{1/6}}{C},$$

where the water depth H is a good approximation for the hydraulic radius R. Wave signals are then measured at numerical wave gauges G_k positioned at $2, 4$ and 6 wave lengths λ, i.e.

$$G_k = 2k \cdot \lambda, \text{ for } k = 1, 2, 3, \qquad \text{with} \quad \lambda = U \cdot T_S$$

We ran numerical simulations with a grid resolution (smallest occurring grid edge) of $\Delta x = 323.60$ resulting from a 13 times uniform refinement of the mesh depicted in Fig. 1. Time integration was performed using Heun's method (RK22) with a CFL number of 0.3 which is close to the theoretical maximum, and the velocity-based slope limiter described in [19]. For the transmissive boundaries at $x \in \{0, L\}$, we followed the work in [1] using Riemann invariants to minimise artificial reflections as treatment of boundary conditions is crucial for simulation accuracy. Overall, and in accordance with [20], we observe a dependence of the wave amplification on the Froude number $\text{Fr} = \frac{U}{\sqrt{gH}}$ with a maximum amplification found at resonance conditions $\text{Fr} = 1$ as exemplarily demonstrated in Fig. 2 for waves measured at wave gauges G_k and in a concise form in Fig. 3.

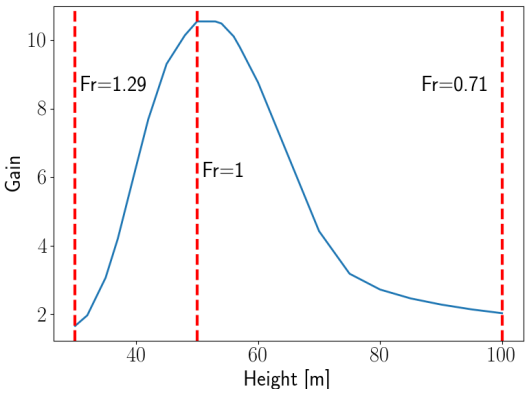

Figure 3: Idealised Proudman Resonance: R1 EXERCISE. Amplification (Gain) versus height H.

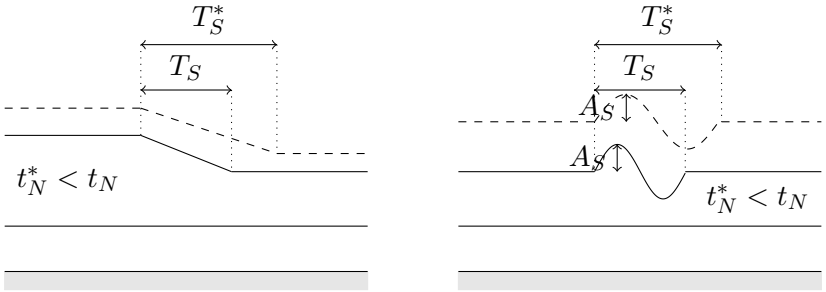

Figure 4: Idealised Proudman Resonance: Relationship of period/steepness of atmospheric disturbance and the normalised time t_N using two different disturbances (solid and dashed) of the same type. Depicted are a linear disturbance (left) and sinusoidal disturbance (right).

3.2 R2 EXERCISE

This exercise explores the non-linear response in wave amplification for different periods T_S of the atmospheric disturbance at resonant water depth and with an otherwise identical set-up to the R1 EXERCISE in Subsec. 3.1. At resonant sea level with Fr = 1 (corresponding to $H = 50$ in our exercise), a linear atmospheric disturbance will lead to an amplification of the form $h_N(t_N) = 2t_N$ as was shown in [9]. Here, t_N is the non-dimensionalised time scale $t_N = t/T_S$. Hence, increasing T_S of a linear disturbance by a factor of 2, halfs the gain in wave height (see also Fig. 4) due to the barometric effect. To investigate amplification for non-linear disturbances, we define a sinusoidal disturbance with period T_S and measure

$$G(t, T_S) = \max_{0 \le t \le t_N T_S} |h(t; T_S)|,$$

where $h(t; T_S)$ is the surface elevation at time t.

We ran simulations using Heun's method (RK22) with a CFL number of 0.3 and a variable time step with 786,432 elements corresponding to a spatial resolution, i.e. diameter of the largest inscribed circle, of about $\Delta r \approx 80.90$. We found high spatial resolution to be necessary

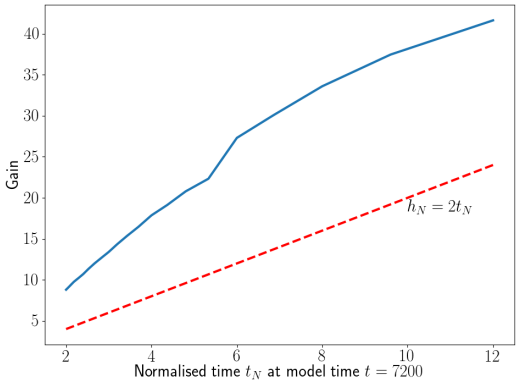

Figure 5: Idealised Proudman Resonance: R2 EXERCISE. Depicted are the linearised increase in gain (red) and the non-linear gain produced with the DG model (blue).

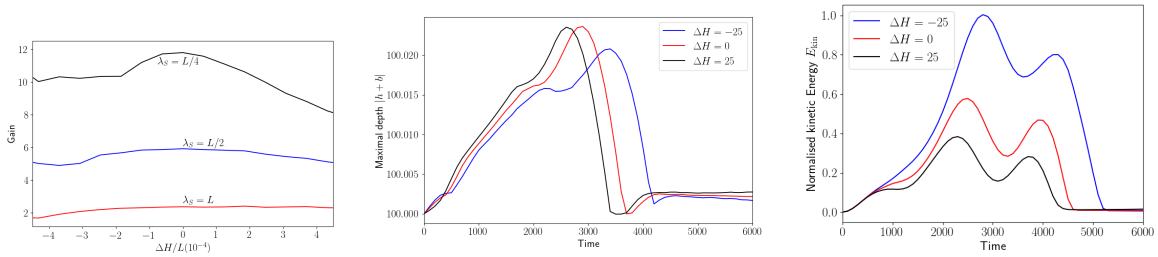

Figure 6: Idealised Proudman Resonance: R3 EXERCISE using different bathymetric slopes ΔH. Depicted are different wave length $\lambda_S = \frac{D}{2}$ (blue),$\lambda_S = \frac{D}{4}$ (black), and $\lambda_S = D$ (red) on the left, maximum total depth (middle) for different ΔH, and kinetic energy (right) for different ΔH.

to guarantee accuracy especially for narrower disturbances. A more detailed discussion of the importance of spatial resolution can be found in Subsec. 3.4.

The averaged gain of our study can be seen in Fig. 5 and shows a larger than linear growth of the maximum wave amplitude due to the non-linearity of the sinusoidal disturbance. In accordance with the findings in [20], we observe a non-linear dependence of the gain in amplitude on the wave length of the disturbance with a higher amplification being observed the more localised the atmospheric disturbance is (larger values of t_N). We furthermore remark a curious feature of the gain curve which is the kink at $t_N = 6$ which corresponds to a significant period of $T_S = 1,200$.

3.3 R3 EXERCISE

Varying bottom topography affects wave amplification. We vary the linear slope ΔH as described in Table 1 of the bathymetry defined by

$$H(x, y) = H_E - \Delta H \left(\frac{2x}{D} - 1 \right), \tag{2}$$

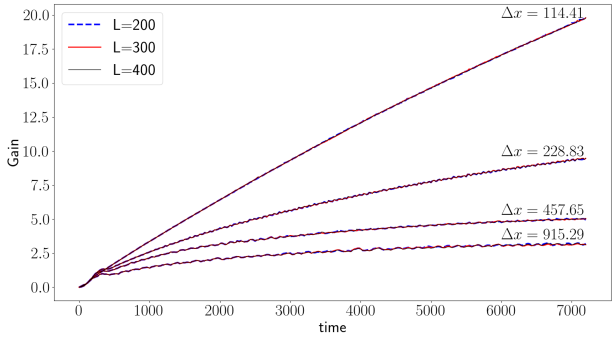

Figure 7: Idealised Proudman Resonance: R4 Exercise with $\Delta H = 0, \lambda_S = 900$, varying resolutions Δx, and domain lengths D (colour-coded).

with $(x, y) \in [0, D] \times [0, \frac{L}{3}]$, $L = 300 \cdot 10^3, D = 81 \cdot 10^3$, $H_E = 50$ (see also Fig. 1). Note, that the R3 EXERCISE is defined on a shorter domain than previous exercises as $D < L$.

We ran simulations with a variable time step and a maximal CFL number of 0.3 using Heun's method. The influence of the interaction between linear bathymetry and size of the atmospheric disturbance can be seen from Fig. 6. For given atmospheric wave lengths $\lambda_S \in \left\{\frac{D}{4}, \frac{D}{2}, D\right\}$, we equidistantly sampled ΔH from $\Delta H \in [-45, 45]$. From Eq. 2, we see that $\Delta H < 0$ corresponds to an increasing bathymetry in travelling direction of the disturbance, causing the water to be deeper on the left side of the domain. The left display in Fig. 6 shows the maximum wave amplification achieved until $T_{\text{end}} = 14,400$ for fixed λ_S. The observed amplification increases with decreasing λ_S indicating that more highly focussed disturbances lead to larger wave amplification. Considering the kinetic energy E_{kin} defined as

$$E_{\text{kin}}(t) = \frac{\rho}{2} \int_\Omega |\mathbf{u}(\mathbf{x}, t)|^2 \mathrm{d}\mathbf{x},$$

we see an increase with decreasing bathymetric slope ΔH as shown in the right display in Fig. 6. This decrease is partly attributed to shoaling effects that decrease wave velocity, and hence kinetic energy. The middle display in Fig. 6 shows maximum wave amplitude over time. Those are larger for negative ΔH where kinetic energy (right display) is smaller because shoaling transforms kinetic into potential energy. Note, that the kinetic energy shows two peaks. The first corresponds to the effects previously discussed while the second is an artefact attributed to the wetting and drying strategy used to model inundation. However, Fig. 6 also suggests a correlation between wave response and domain size, confirming the importance of domain size (or fetch of meteotsunamis) as reported in [22]. To study this in more detail using adaptive mesh capabilities, we have developed the R4 EXERCISE as a special case of R3 with varying domain size.

3.4 R4 EXERCISE: Spatial Resolution

To study the correlation between computational domain size and wave amplification, we simulate the previous test case with a flat bathymetry ($\Delta H = 0$) and a disturbance with wave length $\lambda_S = 900$ for varying domain widths D. until $T_{\text{end}} = 7,200$. The disturbance is initialised with a travel speed of 22.15 and at $x = 20 \cdot 10^3$ to avoid reflections and prevent

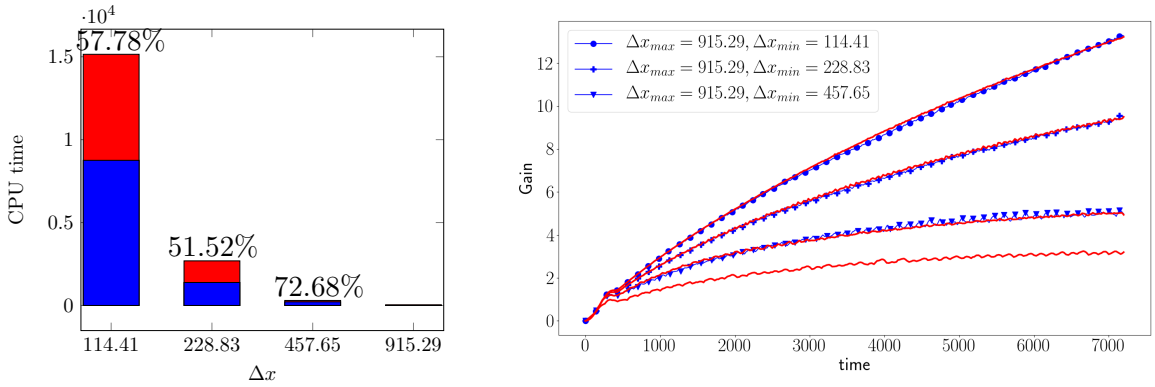

Figure 8: Idealised Proudman Resonance: R4 EXERCISE with $\Delta H = 0, \lambda_S = 900$, and $D = 200 \cdot 10^3$, with varying resolution Δx on uniform and adaptive meshes. CPU time (left) for uniform simulation (red) and adaptive simulations (blue), and amplification for uniform (red) and adaptive strategies (blue) as described in the legend (right).

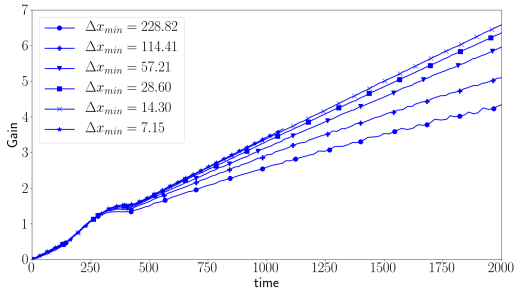

Figure 9: Dependence of gain on spatial resolution for adaptive simulations until $t = 2000$ with $\Delta x_{max} = 228.82$ fixed.

contamination through boundary conditions and reflections. For $D \in \{200, 300, 400\} \cdot 10^3$, we vary spatial resolution, and measure the amplification over time. As we can see in Fig. 7, the amplification changes with spatial resolution, independent of domain size. This confirms that it is important for the atmospheric disturbance to be resolved sufficiently. With a spatial resolution of $\Delta x = 114.41$ this means that the sine wave is resolved with only 8 points. With a large area of hundreds of kilometres this, however means that a very fine resolution might be required for accurate results which is very costly. As mentioned in [21], the spatially localised nature requires a small spatial resolution, hence making practical simulation computationally challenging. However, as the pressure gradients are localised, dynamically adaptive meshes can be beneficial. These meshes can reduce computing time and are especially useful for local high resolution as was demonstrated in [5] for idealised hurricane storm surge.

We refined areas of high water depth gradients using the adaptive mesh capabilities as in Sec. 2 with refinement indicator $\eta_\Omega(t) = \nabla_\Omega \cdot h(\mathbf{x}, t)$. For practicality reasons, we used $D = 200 \cdot 10^3$. The left display of Fig. 8 compares computing time of uniform simulations with resolution Δx as shown (red) with an adaptive simulation with finest resolution $\Delta x_{\text{ref}} = \Delta x$, and a fixed coarse resolution $\Delta x_{\text{crs}} = 915.29$ (blue). The percentages show the fraction of cost of the adaptive simulation relative to the uniform one, stressing that the computing costs are almost halved. The left display of Fig. 8 might suggest divergent results. However, in Fig. 9 we show that with a fine enough resolution numerical convergence is observed. The right display of Fig. 8 shows that the adaptive simulation yields the same wave amplification as the uniform simulation at half the cost. Hence, using the methodology developed in [4] it seems viable to use adaptive simulation for a convergence study.

3.5 R5 EXERCISE: Influence of Bathymetry

The results in Subsec. 3.1 suggest the occurrence of Proudman resonance and with it meteotsunamis in relatively shallow waters. Gently sloping beaching as can be approximated by the R3 EXERCISE in Subsec. 3.3 showed a significant wave amplification. The lack of occurrence of meteotsunamis on rocky coastlines further indicates that local bathymetries impact wave amplification. As an example, there is not a lot of evidence for meteotsunamis on the Irish coasts (see [13]). This has further implication as for example in the context of mega gravel movement, [7] were unable to find any evidence of tsunami waves in recent decades. However, storms occur in those regions that are close to resonant conditions. Using data published in [8] for a winter storm in 2013/14, we deduce that the storm moved 2000km in 24 hours which corresponds to a speed of 23.15. Although being close to resonant conditions for the Irish shelf with an average depth of 50m, no meteotsunami evidence was found - a feature that can be attributed to the bathymetry.

Revisiting old data sets can be challenging though as has been pointed out in [14] due to the relatively low temporal resolution of available data. Hence, the following numerical exercise investigates the influence of a stepped bathymetry onto wave amplification.

As shown in the bottom right display of Fig. 1, we define a stepped bathymetry with $k = 1, 2$ equidistant steps of equal height ΔH_{kS} on the interval $[s_1, s_2]$ and a mean water depth of $H_E = 50$. This is depicted in more detail in the right display of Fig. 10, where we chose $s_1 = 4 \cdot 10^4, s_2 = 8 \cdot 10^4$ and an overall domain length of $L = 10.1 \cdot 10^4$. The atmospheric

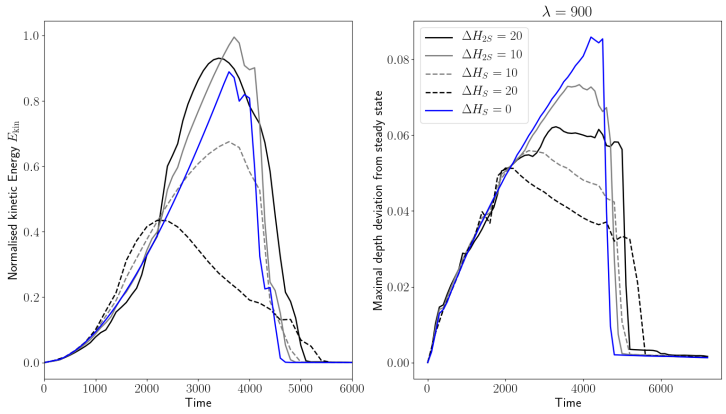

Figure 10: Idealised Proudman Resonance: Kinetic energy over time for R5 EXERCISE over time for different configurations of bathymetry (left) with step height $\Delta H_{kS} = 20$ (black) and $\Delta H_{kS} = 10$ (grey) for $k = 1$ (dashed) and $k = 2$ (solid), and flat bathymetry (blue) as a reference; maximum deviation from initial state over time (right).

Test case		$\max(h + b)$	distance from $x = 8.1 \cdot 10^4$
R5 EXERCISE	$\Delta H_{2S} = 20$	70.0622	$-8,359.37$
	$\Delta H_{2S} = 10$	60.0733	0
	$\Delta H_S = 10$	50.0559	$-23,011.72$
	$\Delta H_S = 20$	50.0513	$-36,246.09$
	$b = 0$	50.0859	0

Table 2: Idealised Proudman Resonance: R5 EXERCISE Location of max total depth.

disturbance is initialised at $x = 2 \cdot 10^4$ to avoid spurious reflections from the transmissive boundary. The results can be seen in Fig.10. On the left we show the normalised kinetic energy. We find that increasing steps increases kinetic energy as shown in the left display. This is due to the mean water depth $H_E = 50$ occurring in the mid point of the domain. Hence, the water depth on the left boundary is higher, the more steps the bathymetry has and so is the gravity wave speed. Comparing to the flat bathymetry (blue line), we can see that stepped bathymetries reduce wave amplification as well as the position where those largest wave heights are found. Due to the linear interaction, the maximum total depth for the R3 EXERCISE is always attained at the right end of the domain. This is in contrary to the R5 EXERCISE. Here, we see in Table 2 that highest wave heights occur away from the shelf, indicating that a stepped bathymetry can reduce meteotsunami threats.

4 DISCUSSION & CONCLUSION

The collection of idealised test cases allows to explore and validate the ability of a model to represent Proudman resonance, which is the dominant source for meteotsunamis. This test suite is capable of detecting sensitivity of the model with respect to resolution, source parameters, and bathymetry characteristics. This suite can only be a start for a comprehensive test suite, which needs to comprise well documented real events.

We have used an adaptive discontinuous Galerkin (DG) model described in Sec. 2 to simulate examples of Proudman resonance, based on the test suite. Using the test cases from [20], we showed that the adaptive DG model in [5] is reproducing a non-linear dependence of wave amplification on several factors: a) the Froude number (with a maximum at $\mathrm{Fr} = 1$) in Subsec. 3.1; b) the temporal period T_S of a non-linear (sinusoidal) disturbance in Subsec. 3.2, as well as c) a negative correlation between steepness of linear bathymetry and wave amplification in Subsec. 3.3.

The observations and results from those three test cases formed the basis to extend the suite of tests to furthermore investigate the influence of spatial resolution on wave amplification as well as influences of stepped bathymetries. In Subsec. 3.4 we found that resolution of the wave is sensitive, in particular fine representation of the source pressure disturbance is necessary. This motivates the use of an adaptive mesh refinement approach. Finally, in Subsec. 3.5 we show that piece-wise linear bathymetries cause an increase in kinetic energy and overall reduce the measured wave heights close to the coast. All above test cases used a simplified, sinusoidal pressure field. Other approximations will be more realistic for practical applications. The application of this model to a more realistic test case is left for a future study.

References

[1] D. C. Antonopoulos and V. A. Dougalis. Galerkin-finite element methods for the shallow water equations with characteristic boundary conditions. *IMA Journal of Numerical Analysis*, 37(1):266–295, 05 2016.

[2] J. Behrens and M. Bader. Efficiency considerations in triangular adaptive mesh refinement. *Philosophical Transactions of the Royal Society A: Mathematical, Physical and Engineering Sciences*, 367(1907):4577 –4589, 2009.

[3] J. Behrens, N. Rakowsky, W. Hiller, D. Handorf, M. Läuter, J. Päpke, and K. Dethloff. amatos: Parallel adaptive mesh generator for atmospheric and oceanic simulation. *Ocean Modelling*, 10(1-2):171–183, 2005.

[4] N. Beisiegel, C.E. Castro, and J Behrens. Quantifying computational efficiency of adaptive mesh refinement for shallow water solvers. *Journal of Scientific Computing*, 87(36), 2021.

[5] N. Beisiegel, S. Vater, J. Behrens, and F. Dias. An adaptive discontinuous Galerkin method for the simulation of hurricane storm surge. *Ocean Dynamics*, 70:641–666, 2020.

[6] D. Belušić and N. Strelec Mahović. Detecting and following atmospheric disturbances with a potential to generate meteotsunamis in the adriatic. *Physics and Chemistry of the Earth, Parts A/B/C*, 34(17):918 – 927, 2009.

[7] R. Cox, F. Ardhuin, F. Dias, R. Autret, N. Beisiegel, C.S. Earlie, J.G. Herterich, A. Kennedy, R. Paris, A. Raby, P. Schmitt, and R. Weiss. Systematic review shows that work done by storm waves can be misinterpreted as tsunami-related because commonly used hydrodynamic equations are flawed. *Frontiers in Marine Science*, 7:4, 2020.

[8] R. Mc Grath. Impact of storm darwin on ireland: description of the event and assessment of weather forecasts. Technical Report 64, Met Éireann, Glasnevin Hill, Dublin 9, 2015. Technical Note.

[9] T. Hibiya and K. Kajiura. Origin of the Abiki phenomenon (a kind of seiche) in Nagasaki Bay. *Journal of the Oceanographical Society of Japan*, 38:172–182, 1982.

[10] A. Jansa, S. Monserrat, and D. Gomis. The rissaga of 15 june 2006 in ciutadella (menorca), a meteorological tsunami. *Advances in Geosciences*, 12:1–4, 2007.

[11] M. Marcos, S. Monserrat, R. Medina, A. Orfila, and M. Olabarrieta. External forcing of meteorological tsunamis at the coast of the balearic islands. *Physics and Chemistry of the Earth, Parts A/B/C*, 34(17):938 – 947, 2009. Meteorological Tsunamis: Atmospherically Induced Destructive Ocean Waves in the Tsunami Frequency Band.

[12] S. Monserrat, I. Vilibić, and A. B. Rabinovich. Meteotsunamis: atmospherically induced destructive ocean waves in the tsunami frequency band. *Natural Hazards and Earth System Science*, 6(6):1035–1051, December 2006.

[13] L. O'Brien, J. M. Dudley, and F. Dias. Extreme wave events in Ireland: 14 680 BP - 2012. *Natural Hazards and Earth System Sciences*, 13(3):625–648, 2013.

[14] C.B. Pattiaratchi and E.M.S. Wijeratne. Are meteotsunamis an underrated hazard? *Phil. Trans. R. Soc. A.*, 373, 2015.

[15] J. Proudman. The effects on the sea of changes in atmospheric pressure. *Geophysical Journal International*, 2:197–209, 1929.

[16] A.B. Rabinovic, I. Vilibić, and S. Tinti. Meteorological tsunamis: Atmospherically induced destructive ocean waves in the tsunami frequency band. *Physics and Chemistry of the Earth*, 34:891–893, 2009.

[17] L. Renault, G. Vizoso, A. Jansá, J. Wilkin, and J. Tintoré. Toward the predictability of meteotsunamis in the balearic sea using regional nested atmosphere and ocean models. *Geophysical Research Letters*, 38(10), 2011.

[18] H. Renqvist. Ein Seebär in Finnland. Zur frage nach der Entstehung der Seebären. *Geografiska Annaler*, 8:230–236, 1926.

[19] S. Vater, N. Beisiegel, and J. Behrens. A limiter-based well-balanced discontinuous Galerkin method for shallow-water flows with wetting and drying: Triangular grids. *International Journal for Numerical Methods in Fluids*, 2019.

[20] I. Vilibić. Numerical simulations of the proudman resonance. *Continental Shelf Research*, 28(4):574 – 581, 2008.

[21] I. Vilibić, J. Šepić, A.B. Rabinovich, and S. Monserrat. Modern approaches in meteotsunami research and early warning. *Frontiers in Marine Science*, 3:57, 2016.

[22] P. Whitmore and B. Knight. Meteotsunami forecasting: sensitivities demonstrated by the 2008 Boothbay, Maine, event. *Natural Hazards*, 74:11–23, 2014.

[23] D.A. Williams, K.J. Horsburgh, D.M. Schultz, and C.W. Hughes. Proudman resonance with tides, bathymetry and variable atmospheric forcings. *Natural Hazards*, 2020.

[24] J. Šepić, L. Denis, and I. Vilibić. Real-time procedure for detection of a meteotsunami within an early tsunami warning system. *Physics and Chemistry of the Earth, Parts A/B/C*, 34(17):1023 – 1031, 2009. Meteorological Tsunamis: Atmospherically Induced Destructive Ocean Waves in the Tsunami Frequency Band.